the radial velocity of the probe tip is directed away from the drogue wall that is initially contacted. The docking hardware sustained the imposed dynamic loads without failure or malfunction, although several latching anomalies occurred during case 1 and 3 testing. These events were attributed to repeated use of the probe assembly at high energy levels which were not indicative of actual flight conditions. Math model data with inputs for flight vehicle mass properties and 6 degrees of freedom compared favorably with experimental data for all test cases. In general, correlation improved as the energy of the various systems of docking vehicles increased. The astronaut training film consisted of a split-frame view showing the COAS reticle pattern superimposed over the opposing vehicle target, combined with a view of the probe/drogue behavior (Fig. 4). This combination of views provided the astronauts with their first opportunity to simultaneously observe a time-correlated accounting of the two events. A composite film depicting the various test conditions is reviewed by primary crew members prior to each Apollo mission.

Full-Scale Apollo Docking Simulation Tests

JAMES F. SILLER*
McDonnell Aircraft Company, St. Louis, Mo.

Transposition and lunar docking associated with Apollo 9 and subsequent manned Apollo missions were simulated using test vehicles equipped with flight-type docking hardware. Flight vehicle mass properties were simulated and each test vehicle was provided with 5 degrees of freedom, except for the heavy Apollo 9 LM/SIVB vehicle which was simulated by a fixed structural frame. The test vehicles were suspended as simple pendulums with each suspending cable terminating at the vehicle CG in a three-axis gimbal system. The overhead pendulum pivots were supported on air bearings. Program objectives included latch capture boundary studies, demonstration of docking hardware capabilities, experimental and math model data comparisons, and the procurement of astronaut training aids via film documentation of the docking targets as viewed through the Crewman Optical Alignment Sights. Variable test parameters included velocity, attitude, angular rate, radial miss distance, and longitudinal thrust applications.

Nomenclature

COAS	=	crewman optical alignment sight
CSM	=	command and service module
Ek	=	kinetic energy
I	=	mass moment of inertia
LM	=	Lunar Module
LM/SIVB	=	Lunar Module/Saturn IVB
M	=	mass
R	=	radial miss distance
r	=	distance from initial impact point to vehicle CG
V	=	resultant velocity of CSM probe tip
$\dot{X}$	=	vehicle longitudinal velocity
$\ddot{X}$	=	vehicle longitudinal acceleration
$\dot{Z}$	=	vehicle radial velocity
α	=	angle between CSM probe tip resultant velocity vector and drogue wall
θ	=	relative angular misalignment of vehicles' longitudinal axes
$\dot{\theta}$	=	vehicle angular velocity

Subscripts

1	=	CSM
2	=	LM or LM/SIVB

Introduction

FULL-SCALE Apollo docking tests were conducted using vehicles which simulated the CSM, LM, and LM/SIVB. The program was divided into three phases simulating the following missions and related docking vehicles: 1) transposition docking of the Earth-orbital Apollo 9 mission (case 3—CSM docking with heavy LM/SIVB), 2) lunar orbit docking (case 2—docking between the LM and CSM following lunar rendezvous), and 3) normal transposition docking associated with Apollo 10 and successive missions (case 1—CSM docking with LM/SIVB during translunar coast).

Each test vehicle incorporated flight-type docking subsystem components that were mounted on a steel framework and, except for the case 3 LM/SIVB, each vehicle was provided with three angular and two translational degrees of freedom through a gimbal system and air bearing assembly, respectively. The case 3 LM/SIVB vehicle was simulated by a fixed structural frame.

The program included the following test objectives: a) to determine the latch capture boundary conditions, b) to ascertain the structural and functional integrity of the docking hardware in a dynamic environment, c) to compare experimental and math model data, and d) to provide the astronauts with visual training aids via film coverage of the tests through the COAS depicting the docking vehicle behavior at and following initial contact.

Vehicle initial contact test parameters included longitudinal closing velocity, radial velocity, angular velocity, angular misalignment, radial miss distance, and longitudinal thrust/no-thrust conditions. Automatic and manually-initiated CSM probe retractions were demonstrated following latch capture during three test runs. The test vehicles were instrumented to record translational and angular accelerations, planar excursions, angular rates and attitudes, and longitudinal thrust magnitude. The probe assembly was instru-

Presented as Paper 70-170 at the AIAA 8th Aerospace Sciences Meeting, New York, January 19–21, 1970; submitted February 19, 1970; revision received April 27, 1970. This work was supported by NASA under contract NAS9-9004.

* Group Engineer, Structures and Dynamics Laboratories.

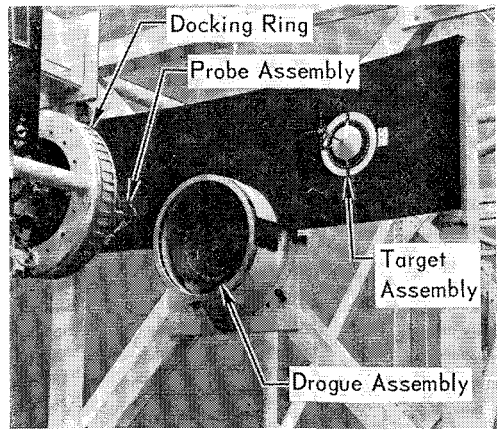

Fig. 1 Case 1 test setup.

mented to obtain structural loads and probe stroke. A total of 135 test runs were completed.

Description of Test Articles

Each test vehicle, except the case 3 LM/SIVB vehicle, consisted of a ballasted steel framework with a three-axis gimbal system located at its CG. The docking subsystem components were mounted on the steel frameworks. The mass properties of the test vehicles were as shown in Table 1 and are representative of flight vehicle mass properties within a maximum deviation of 0.1% and 2.1% for the required weights and inertias, respectively. Test vehicle CG locations were within 0.1 in. of the required three-axis coordinates. Weights and CG locations were experimentally determined and inertias were analytically determined.

Docking Subsystem

The docking subsystem included the probe assembly and docking ring for the CSM and the drogue assembly with attach fittings for the LM or LM/SIVB. The role of the probe assembly during the docking maneuver is to dissipate the kinetic energy of the closing vehicles, control post-contact dynamics, provide initial mechanical coupling, limit vehicle misalignments, and provide retraction forces during the rigidizing cycle. The docking ring serves as a mounting base for the probe assembly and provides an interfacing, sealing surface between the docking vehicles during retraction and rigidization.

The drogue assembly has the shape of a truncated cone and presents a target profile wherein initial probe contact may occur. The drogue subsequently guides the probe tip to its apex where latch capture is effected. Latch capture provides the initial mechanical coupling between the vehicles and is achieved when all of the three latches housed in the probe tip snap over the edge of the truncated drogue cone.

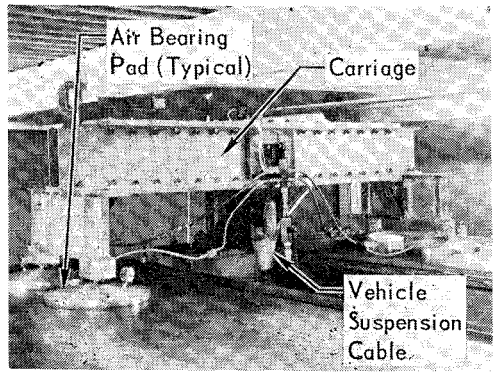

Fig. 2 CSM air bearing-carriage assembly.

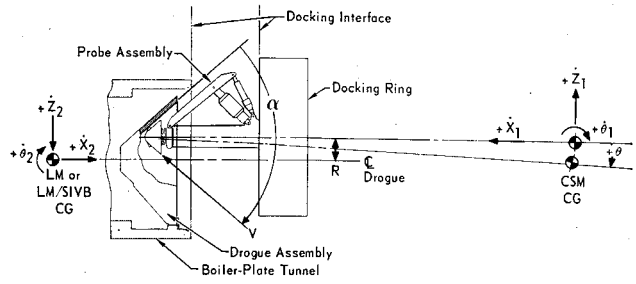

Fig. 3 Test parameter legend (conditions at initial impact).

The drogue assembly will dissipate energy during the docking cycle if velocities and attitudes cause deformation of the drogue aluminum honeycomb substructure. Narrow, concentric rings were painted on the drogue inner surface using chalk water and served as a frame of reference during film and video analyses to relate probe position to the drogue. The rings were not a part of the flight hardware configuration and were not considered detrimental toward altering the probe/drogue coefficient of friction due to the small drogue area which they covered. The leading edge of the boiler plate tunnel assembly in which the drogue assembly was mounted simulated flight vehicle contours. Tunnel leading edge contours were simulated since this surface could be involved in post-contact dynamics with the vehicles angularly misaligned or, for test conditions where the probe tip would pass in the immediate vicinity of the tunnel leading edge, undue interference could occur without the proper contours. The docking subsystem is visible in Fig. 1.

Auxiliary Test Devices

Longitudinal thrust and angular acceleration forces applied to the test vehicle were achieved by the use of onboard, cold-gas (air) thrusters, except during case 3, when longitudinal thrust was applied to the CSM through a cable attached to a falling weight. Air for the thrusters was applied from an off-board source, except during case 3, when air bottles mounted on the CSM powered the angular rate thrusters.

A simulated COAS was mounted on the CSM test vehicle for all test cases and on the LM vehicle during case 2 tests. The COAS was simulated by a projection system which optically superimposed a reticle pattern over its opposing vehicle target assembly. The combined reticle/target image was viewed by an onboard 16-mm cine camera located at the crewman's eye position. Reticle pattern design, color tone, and component geometry were faithfully reproduced since these films were to be used as training aids. A beam-splitting mirror, incorporated in the simulated COAS, allowed simultaneous viewing of the reticle/target image by an onboard television monitor. A 16-mm camera and television monitor were also mounted forward on the CSM to view probe/drogue interaction.

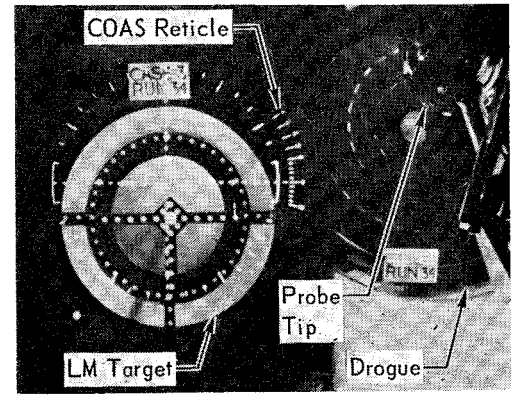

Fig. 4 Split-frame training aid view.

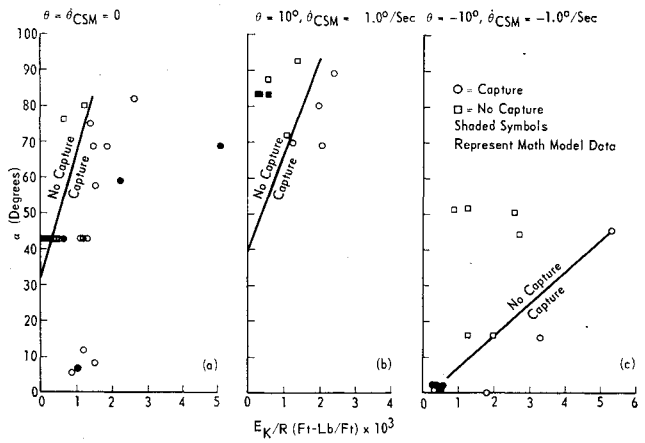

Fig. 5 Latch capture boundaries for case 1 (no-thrust).

Since the flight-type target assembly on the LM vehicle contains radioactive, fluorescing units to aid in visual tracking when the sunlight is obscured, a mockup target was used during the program to avoid the handling problems inherent to the radioactive flight unit. The illuminated CSM target assembly was used only during the simulated lunar orbit docking of case 2, when longitudinal thrust was applied to either the LM or CSM vehicles. Exact geometric relations between the docking subsystem components and target assemblies were maintained.

Onboard instrumentation included probe load-stroke transducers, accelerometers to monitor vehicle translational and angular acceleration, longitudinal thrust force transducers, and angular rate and attitude gyro packages. Instrument outputs were connected to offboard recording equipment through a wire bundle, rigged to offer minimum restraint to the test vehicles.

Case 3 Test Vehicles

The Apollo 9 LM/SIVB vehicle was simulated by a rigid steel frame attached to the laboratory floor because it was not practical to simulate the 222,384-lb weight of the flight vehicle. The drogue and tunnel assemblies were mounted on the face of the rigid frame and the mass properties of the CSM test vehicle were scaled down to compensate for the near-infinitely rigid LM/SIVB test vehicle. Since coupling full-scale CSM mass properties with a rigid simulation of the LM/SIVB vehicle would have required that the docking subsystem absorb 30% more energy, scaled-down CSM mass properties were used to avoid inducing artificially high-loads in the docking subsystem and to obtain correct postimpact velocities. The geometric relationship between the CSM CG and the probe assembly was not altered. CSM longitudinal thrust was scaled down by an amount equal to the ratio of test vehicle mass to flight vehicle mass.

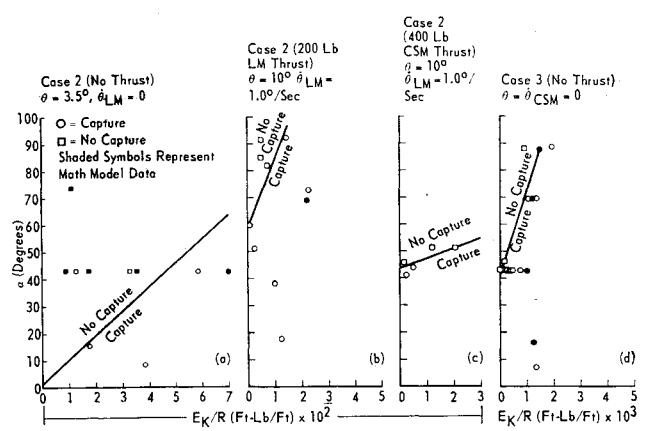

Fig. 6 Latch capture boundaries for cases 2 and 3.

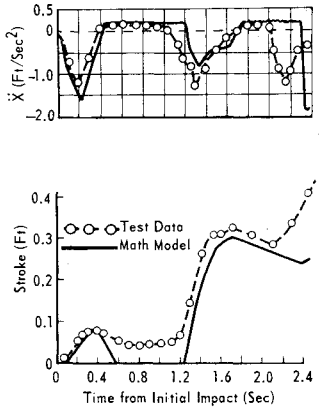

Fig. 7 Case 3, Run 40b, CSM CG acceleration and probe stroke.

Impulse-momentum equations were written for two impacting free-bodies and for a free-body impact against a fixed surface. Equating separation velocities and impulsive forces for the two conditions resulted in the following equivalent mass property equations:

$$M = M_1M_2/(M_1 + M_2) \quad (1)$$

$$I = I_1I_2/[I_2 + I_1(r_2/r_1)^2] \quad (2)$$

Test Procedures

Each test vehicle, except for the case 3 LM/SIVB, was suspended as a simple pendulum with the suspending cable attached to the vehicle at the CG-oriented gimbal assembly. The pendulum lengths, measured from the upper pivot to the gimbal trunnions, were approximately 56 ft with the lower $\frac{1}{3}$ of each suspension cable considered as effective vehicle mass. The overhead pendulum pivot point for each test vehicle was supported by an air bearing-carriage assembly. The air bearing for the CSM, which was identical to the case 1 LM/SIVB air bearing, is shown in Fig. 2. The air bearing for the case 2 LM was similar in construction, but lighter in weight. The mass of each air bearing-carriage assembly was minimized to reduce its effect on the dynamic behavior of the docking vehicles and the lateral translations and accelerations of each air bearing were recorded on a time base common to their respective test vehicle instrumentation outputs so that the air bearing mass loading effects could be evaluated.

During any test, only one vehicle was active and the other vehicle was passive. Energy was induced in the system by displacing the active vehicle horizontally with its overhead air bearing restrained. The displaced vehicle was then released and allowed to contact the passive vehicle. The air bearing restraint was removed when the active vehicle had attained maximum velocity. The CSM was active during test cases 1 and 3 and the LM vehicle was active during case 2 tests in that it was always the displaced vehicle. However, there were case 2 test conditions which involved the application of longitudinal thrust to the CSM vehicle. Due to the disparity in weights of the case 2 test vehicles (5670 vs 35,130 lb), closing velocities were always induced in the lighter LM vehicle to reduce the amount of energy in the system and limit post-impact vehicle excursions.

Diametrically opposed thrusters applying a known torque on the active vehicle were fired during test runs requiring

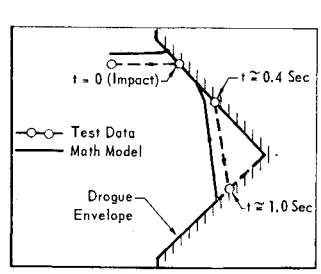

Fig. 8 Case 3, Run 40b, CSM probe tip excursion.

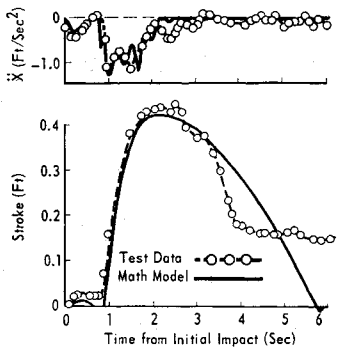

Fig. 9 Case 3, Run 33, CSM CG acceleration and probe stroke.

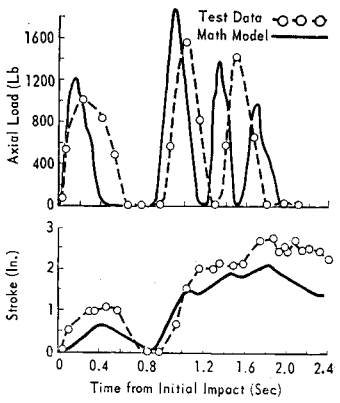

Fig. 10 Case 1, Run 7, CSM probe axial load and stroke.

angular velocity. The thrusters were actuated during the vehicle/pendulum swing and the time required to accelerate to a maximum angular velocity was less than the pendulum quarter-period.

Longitudinal thrust applied to a test vehicle was automatically initiated at probe/drogue contact and was maintained for a period of 4 sec or until probe capture, whichever occurred first. Thrust initiation was sequenced with release of the active vehicle and, through the use of time-delay circuitry, was deferred by an interval equal to the vehicle/pendulum quarter-period. Thrust magnitudes were 200 lb (LM case 2), 320 lb (CSM case 3), and 400 lb (CSM cases 1 and 2).

Longitudinal and radial velocities were varied by adjusting the displacement of the restrained active vehicle prior to testing. Maximum required values were 1.0 fps and ±0.5 fps for the longitudinal and radial velocities, respectively. Required miss distances for initial impact of the probe tip on the drogue wall, measured radially (normal to the longitudinal axis), ranged up to 12 in. Maximum values for angular misalignments and angular velocities were ±10° and ±1.0 deg/sec, respectively. Positive-value test parameters are defined in Fig. 3. Automatic probe retraction following latch capture was demonstrated twice during case 2 testing. Probe retraction was manually initiated during one case 1 test.

Motions induced in the test vehicles, other than those resulting from impact, were restricted to the horizontal plane. The CSM vehicle pitch axis was vertical during case 1 and 3 testing; therefore, all induced angular motion resulted in a pitching maneuver. The LM vehicle pitch axis was vertical during case 2 tests and since the y-z axes of the two aligned and docked vehicles are angularly displaced by 60°, the CSM vehicle was rolled through the 60° angle for case 2 tests. The test configuration for case 1 is shown in Fig. 1.

Colored films from the two onboard cameras showing the COAS reticle/target image and probe/drogue interaction were processed into a time-correlated, split-frame presentation for use as an astronaut training aid. The reticle/target view occupied 60% of the frame and the probe/drogue view occupied the remaining 40%. An excerpt from the split-frame film is shown in Fig. 4. Views for the onboard television monitors were arranged in a split-screen display duplicating the 16-mm film presentation. Television monitor outputs were taped and available for split-screen review immediately following each test run. The television instant replay was a valuable aid enabling the test engineer to make motion studies and rapidly define succeeding test parameters.

Deviations from the existing test plan that were required during the program were discussed and formulated by a Test Review Board which included representatives of NASA, McDonnell Douglas Corp., and North American Rockwell Corp.

Test Results

Because of the rigid scheduling of the program and the vast amount of data to be analyzed, only selected conditions could be tested. Therefore, capture boundaries have been defined only for conditions where a sufficient number of tests were conducted to validate the definitions. The capture boundary data as presented here relates the angle that the CSM probe tip resultant velocity vector makes with the drogue wall (α) vs the ratio of the total kinetic energy of the active vehicle to the radial miss distance (Ek/R). Test parameters are shown in Fig. 1. The ratio of kinetic energy to radial miss distance was used to reduce several parameters ($\dot{X}$, $\dot{Z}$, $\dot{\theta}$, and R—see Fig. 1) into a single expression so that a two-dimensional coordinate system could be used, when combined with α, to define the capture boundaries. Conditions were based on values existing at initial impact. The capture boundaries are shown in Figs. 5 and 6 for combinations of angular attitude and velocity and for thrust/no-thrust conditions. Latch capture boundaries were defined in a different manner in Ref. 1 (Vol. 4) where plots of longitudinal velocity versus radial miss distance are presented. The plots were categorized for single values of radial velocity, angular velocity, angular attitude, and thrust or no-thrust applications.

The functional and structural integrity of the docking subsystem were successfully demonstrated. However, repeated use of the probe assembly at high energy levels during test cases 1 and 3 caused individual capture latches to seize within the probe tip housing. While it was felt that the capture

Table 1 Test vehicle mass properties

Test case	Test vehicle	Weight, lb	CG location, in. (Apollo coordinates) x[a]	y	z	Moment of inertia, slug-ft² Ixx	Iyy	Izz
3	CSM	46,760	176.45	3.7	6.0	23,900	62,700	65,000
	LM/SIVB		Not applicable					
2	CSM	35,130	165.85	1.4	5.7	18,000	53,700	58,800
	LM	5,670	55.45	3.8	−2.2	3,140	2,780	1,910
1	CSM	65,400	175.05	3.8	6.5	33,900	80,500	82,900
	LM/SIVB	65,600	337.35	1.3	3.3	98,200	1,038,100	1,038,100

[a] Longitudinal dimension measured from the docking interface plane. See Fig. 3.

Table 2 Experimental and math model test conditions at initial impact[a]

Case	Run	Active vehicle	R, in. Math model	R, in. Test	$\dot{X}$, fps	$\dot{Z}$, fps	θ, deg	$\dot{\theta}$, deg/sec	Thrust
3	40B	CSM	12.0	10.5	1.0	0.5	−10.0 −10.8 (Test)	1.0	CSM
3	33	CSM	9.0	9.1	1.0	−0.5	0	0	None
2	17	LM	11.0	10.8	1.0 0.9 (Test)	0	3.5	0	LM
1	7	CSM	9.0	9.3	1.0	0	0	0	None

[a] Test and math model conditions are the same except as noted—see Fig. 3.

latch seizure precipitated by the repetitive high loadings was not indicative of actual flight conditions, in-line inspections were instituted by NASA and minor latch design changes were made to the flight hardware. Splitting of the drogue cone inner skin, experienced during case 3 high energy level tests, was attributed to capture latch seizure. Automatic and manually-initiated probe retractions following latch capture were demonstrated without malfunction or erratic vehicle behavior.

A sampling of the correlation between math model data and experimental data is shown in Figs. 7–11. The NASA math model was used to generate analytical data for the correlation. Conditions at initial impact are defined in Table 2 for the test runs illustrated. Two objectives were to establish correlation based on a math model representative of the case 3 test setup (scaled-down CSM mass properties, rigid LM/SIVB, 5 degrees of freedom) and to establish correlation of all test case results with math model data representative of the flight vehicle docking dynamics (true mass properties, 6 degrees of freedom).

The first objective was satisfied and is partially illustrated by Figs. 7 and 8. In these figures, representing case 3, Run 40B, comparisons of data are shown based on math modeling that included very large LM/SIVB mass properties, scaled-down CSM mass properties, and elimination of the sixth (vertical) degree of freedom. The math model inputs for the LM/SIVB were 10^7 slugs and 10^6 (roll) and 10^8 (pitch and yaw) slug-ft^2 for the mass and mass moments of inertia. CSM mass property inputs were as defined in Table 1. The data for this comparison were derived from the NASA docking math model digital computer program and were provided by the North American Rockwell Corporation. The difference in radial miss distances between Run 40B and the math model input accounts for a progressive time shift of the second and third probe/drogue impacts as illustrated by the acceleration curve of Fig. 7. This condition is further clarified by observing the predicted and actual probe tip excursions shown in Fig. 8. The indication of approximately $\frac{1}{2}$ in. of probe stroke shown in Fig. 7, when the stroke should have returned to zero, may be attributed to mechanical play in the probe linkages, which the computer program did not include.

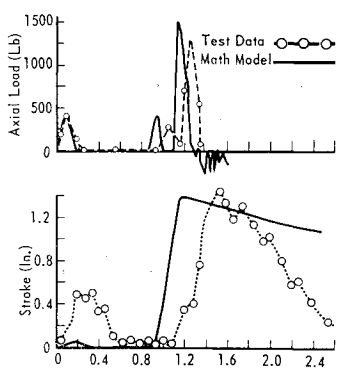

Fig. 11 Case 2, Run 17, CSM probe axial load and stroke.

The second objective, to correlate the three test case results with flight vehicle math model data, was accomplished as demonstrated by Figs. 9–11. The data for these comparisons were supplied by NASA and are based on the same math model program used for the case 3, Run 40B analysis, except that inputs included flight vehicle mass properties and 6 degrees of freedom. The case 3 CSM and LM/SIVB math model inputs simulating flight vehicle mass properties were approximately: CSM, 1.84×10^3 slug, 3.17×10^4, 7.87×10^4, and 8.31×10^4 slug-ft^2 (roll, pitch, and yaw, respectively); LM/SIVB, 6.95×10^3 slug, 1.07×10^5, 2.334×10^6, and 2.336×10^6 slug-ft^2 (roll, pitch, and yaw, respectively).

Good correlation was obtained for Run 33 of case 3 as shown in Fig. 9, which established the validity of the test approach used in case 3 (rigid LM/SIVB and effective CSM mass properties). The probe stroke deviation shown in Fig. 9 was caused when the probe tip remained in contact with the initially impacted drogue wall instead of skipping off at a very shallow angle as derived in the math model simulation. The probe load phase shift of Fig. 10 may be attributed to the slightly larger miss distance of Run 7, case 1 and to a greater than anticipated drogue local deformation. Permanent deformation of the drogue would also attenuate the initial, peak probe loads. The secondary impact phase shift of Run 17, case 2 shown in Fig. 11 was caused by the low initial velocity (0.9 vs 1.0 fps) of the LM test vehicle. The approximate $\frac{1}{2}$ in. of probe play is again apparent during Run 17 as shown in Fig. 11.

The split-frame color films for all test cases were transmitted to NASA for formal training film applications and were subsequently reviewed by the Apollo astronauts. The films exist as training aids, as identified in Ref. 2 and 3, and are reviewed by primary crew members prior to each Apollo mission. The split-frame films were initially used in preparation for the Apollo 9 flight.

Data are presented for test cases 1–3 in Ref. 1, which includes plots of the following parameters versus time: probe attenuator, tension link, and shock strut loads; probe piston and attenuator strokes; test vehicle CG acceleration, angular acceleration, angular velocity, angular attitude, x-y excursion, and longitudinal thrust; test vehicle air bearing-carriage acceleration, angular attitude, and x-y excursions.

Conclusions

Docking maneuvers, wherein the radial velocity of the active vehicle tends to direct the probe tip away from the drogue wall that is initially contacted, broaden the latch capture boundaries. This condition would result in a lower value for α for Figs. 5 and 6, where it may be seen that a larger portion of the capture regime enclosed by the boundary curve lies. The application of vehicle longitudinal thrust also improves capture capabilities as may be seen by comparing (a) and (b) of Fig. 6.

The docking subsystem sustained the imposed dynamic environment without structural failure or malfunction, other than the off-limit anomalies described in the test results section.

Experimental data closely agreed with math model data for those tests investigated which confirmed both the dynamic simulation of the docking vehicles and the test techniques employed. This type of certification was of vital concern during all modes of testing, but was especially significant during case 3 testing when CSM mass properties were scaled down to accommodate the rigid frame simulation of the LM/SIVB. Correlation of experimental and math model data improved as the size of the docking vehicles increased. That is, correlation was best during case 3, followed by the order of cases 1 and 2. In general, correlation improved as the energy of the various systems of docking vehicles increased, tending to negate factors unique to the test setup which might compromise the simulation of flight conditions (friction, air bearing mass, one-g field, etc.).

Because the field of view through the COAS is restricted to the target and adjacent areas with the docking vehicles aligned and in close proximity, the split-frame film coverage from the Apollo docking tests afforded the astronauts their first opportunity to simultaneously observe the target as viewed through the COAS, time correlated with the probe/drogue activity.

References

[1] "Apollo Full-Scale Docking Simulation Tests," G962, May 1969, Vols. 1–4, McDonnell Douglas Corp., St. Louis, Mo.

[2] "Apollo Docking Pendulum Tests," Film MSC-69-521, NASA-MSC, Houston, Texas.

[3] "Apollo Docking Dynamics," Film MSC-69-521R, NASA-MSC, Houston, Texas.